# Chapter 3

# Shape measurement of phase object and quantitative 3D imaging of dynamic micro-objects using fringe projection technique

## 3.1 Introduction

Optical metrology is the science and technology of making measurements of variety of variables and quantities and drawing significant conclusions from a large data set with the help of light based techniques for measurement [194–197]. It wasn't until recent advancements in the optics, computers and information processing techniques that masses have finally begun to harness the true power of optical metrology [198]. Real time three-dimensional shape measurement, fast and powerful computers, high resolution sensors, quick data processing capabilities and have all led to development in various forms of optical metrology and it find its application in various fields such as testing of military optical system [199] automotive [200], biomedical [198], semiconductor [201], and aerospace [202] etc. It is quickly becoming popular especially due to its non-invasive nature with ease of setup, fast data acquisition and remote sensing options also available [203].

Many techniques are developed and used over the years, and the field of optical metrology for measurement has seen significant advancement [203–205]. There are whole field techniques that include holography and hologram interferometry [174,206,207], speckle photography and speckle interferometry [208–210], moire interferometry [211,212], photoelasticity [19, 20], microscopy [40,42,215,216], fringe projection techniques [25,26]. All these techniques are extensively for deformation studies, vibration analysis and surface [194].

Fringe projection, a non-interferometric, non-invasive technique for generating 3D surface information, has gained a lot of attraction in optical metrology in recent years [133]. This technique has found various applications in different areas: biomedical applications such as 3D intra-oral dental measurements [217], non-invasive 3D imaging and monitoring of vascular wall deformations [218], human body shape measurement for shape guided radiotherapy treatment [29,30] lower back deformation measurement [221], detection and monitoring of scoliosis [222], inspection of wounds [33, 34] and skin topography measurement for use in cosmetology [35,36]; industrial and scientific applications such as characterization of MEMS components [37,38], vibration analysis [39,40], refractometry [231], global measurement of free surface deformations [42,43], corrosion analysis [234,235], measurement of surface

roughness [46,47], reverse engineering [48,49], quality control of printed circuit board manufacturing [50,51] and heat-flow visualization [242]; kinematics applications such as measuring the shape and position of a moving object/creature [53,54]; biometric identification applications such as 3D face reconstruction for the development of robust face recognition systems [245]; cultural heritage and preservation [56,57] etc.

A projection unit, an image acquisition unit, and a processing unit make up the Fringe Projection Technique (FPT). The 3D shape measurement device is divided into two sections [25, 58]. On the object surface, the projection unit projects a structured pattern (sinusoidal or grid pattern). The image of the fringe pattern modulated by the object height distribution is recorded, and this phase modulation is calculated by performing Fourier fringe analysis on the fringe to generate a wrapped phase distribution. To obtain a continuous phase distribution, an appropriate phase unwrapping algorithm is implemented, and the system is calibrated for mapping the unwrapped phase distribution. Fringe projection method is used in transmission mode and triangulation method is used in reflection mode.

Fringe projection technique is most suitable for contouring objects having too large height variations to be measured with standard interferometry [134]. To contour an object, simply project sinusoidal fringes onto it and then look at it from a different angle. An image capturing sensor records a distorted fringe pattern that has encoded the information about the object's depth [205]. For best results, the image plane should be normal to the direction of projection of light beam. The surface height with respect to the reference surface can be quantified using phase-measurement techniques. The reference surface will be a plane if the contour lines are straight and evenly spaced in object space. By using a simple Fourier transform based fringe analysis technique, any desired plane can be deducted from the obtained surface height to yield the surface profile relative to any plane (or surface). The number of fringes in the sinusoidal pattern will determine the precision of surface-height measurement. In the reflection mode, the resolution is determined by the triangulation angle, the pixel size of the sensor and distance of the sensor to the nodal point of the camera objective. The advantages of the structured light method are as follows: (1) simple implementation; (2) no moving parts required for phase shifting, fringe density, or fringe orientation change; and (3) quick full field measurement (4) For the projection of a structured pattern, any light source can be used. The coordinate measurement and machine vision industries have begun to commercialise the

structured light method as a result of these benefits, and some promising applications can be found in the literature [60,61].

The main difference between holographic interferometry techniques and fringe projection is the fact that structured light is projected directly on the object under investigation in Fringe Projection Technique (FPT) and in interferometry techniques the fringes are created due to path length difference between reference beam and object beam [10,63]. Coherent light source is required in interferometry techniques while any light source can be utilized to project the line pattern on the object with sufficient intensity. Several advantages that fringe projection technique offers over interferometry are: the technique has a simple, compact and inexpensive configuration, and there is no need of stringent beam alignment as is required in interferometry techniques [248].

Fringe projection can be used in two configurations: reflection and transmission mode. In transmission mode, structured light pattern is transmitted through the specimen and the distorted pattern is viewed directly behind the object i.e. perpendicular to the projection direction [249]. Fringe Projection technique can even be applied for opaque objects. Structured pattern is projected on the opaque object and the distorted pattern is imaged and surface modulation is reconstructed. This is known as reflection mode Fringe Projection [250].

### 3.2 Transmission mode Fringe Projection Technique

In case of transmission mode FPT, where the fringes projected pass through the object, the fringe modulation occurs due to spatially varying optical path length. This gives rise to deviation of light towards higher optical thickness or higher optical path length [66,67]. In an axi-symmetric object (for example a converging lens), this will give rise to symmetric fringe deflection towards region of higher optical thickness i.e. towards region of higher thickness multiplied by the refractive index (RI) of the lens material, hence giving rise to equal modulation of fringes on both sides of the axis, symmetrically [253].

Fig 3.1 Recorded modulation of line pattern projected through a lens.

Fig 3.1 shows the modulation of structured pattern (here line pattern) through lens which is a phase object [254]. One can observe the symmetric nature of deflection of fringes relative to the optical axis. The non-uniformity of thickness distribution of the lens can be seen from the deviation of fringes. When the phase obtained from this modulation is compared to the straight lines in the background, information about gradient of optical thickness of the lens along the direction of thickness variation is obtained. This phase gradient must be integrated along the direction of optical path length gradient obtained, to get the thickness and/or refractive index variation.

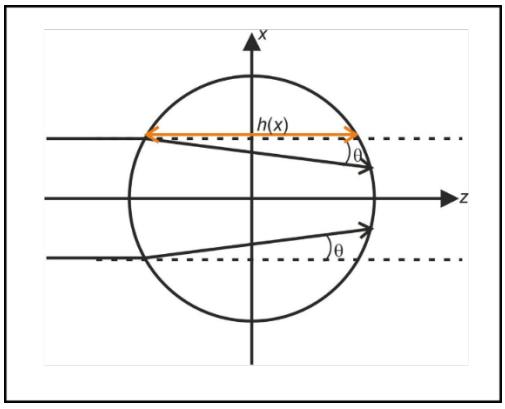


Fig 3.2 Propagation of light through axi-symmetric object

Fig 3.2 shows the propagation of a light ray through spherical object (circular cross-section) having spatially varying optical thickness. The ray, as discussed will deflect towards region with higher optical thickness.

Consider optical path length change along x-direction. The angle of deflection in z-direction (light propagation direction) can be denoted by, [253,255]

$$\frac{d}{dx}\left(n\frac{dx}{dz}\right)=\frac{\partial\Delta(x,t)}{\partial x} \tag{3.1}$$

Where, Δ is the optical path length given by, $\Delta = n \times h$, $n$ is the RI and $h$ is the thickness and $x$ is the direction of optical path length change

This equation can be simplified by assuming the angle of deflection to be small and constant RI, providing the equation of angle of bending as

$$\theta(x,t)=\frac{h(x,t)}{n}\frac{\partial\Delta(x,t)}{\partial x} \tag{3.2}$$

Since a light ray will bend more towards the surface normal while transitioning from a region of lower refractive index to higher refractive index region and amount of bending depends on the gradient of optical path length, from Eq. (3.2), we obtain the angle of deflection of light, which in turn can be used to determine the thickness of the specimen at a given time instance $h(x, t)$.

### 3.3 Shape Measurement of Phase Objects using Fringe Projection Technique

Study presented in the thesis is focused on shape measurement of transparent optical components such as wedges, lenses, and cylindrical rods by fringe projection technique and later on its use in imaging of transparent micro-objects like blood cells. Structured pattern of parallel alternate dark and bright bands are printed on a normal paper (75 gsm) using laser printer. The objects discussed above are phase objects and hence, transmission mode setup has been devised i.e. the pattern is projected through the specimen under investigation using an LED light source. The pattern is modulated by the specimen and this modulation is captured by imaging system, consisting of imaging lens and an arrayed digital sensor. This pattern is recorded into the computer and later Fourier analysis is carried out to extract the optical thickness profile of the object. The advantage is that less optical components are required in this configuration and the results may be comparable with interferometry methods. The developed setup can be further developed into a compact instrument.

#### 3.3.1 Experimental Setup

The experimental setup of Fringe Projection Technique (FPT) for 3D shape measurement of transparent objects is shown in Fig 3.3. An LED with central wavelength $\lambda_c$= 627 nm and line width of 20 nm having output power of 2 W is used as the source. The light from LED falls on the 100 mm $\times$100 mm structured light pattern which is a set of parallel lines with pitch 0.5 mm printed on a paper. The lines are designed are scaled and is printed on paper using Inkjet laser printer. The intensity variation in pattern is sinusoidal in nature (Fig3.4). The light from LED

source illuminates the line pattern and goes through the pattern. The object to be investigated is placed behind the line pattern. This object deforms the fringe pattern due spatial variation of optical thickness, so that the projected straight line is modulated wherever the object is present. The image sensor is kept behind the object under investigation. The CCD (Thorlabs, pixel pitch 4.65mm) and a smartphone camera is used as sensor to record the image of the interference pattern projected through the object. The fringes are distorted by the object and these distorted fringes can be recorded by these sensors. Fig 3.5 (a). shows 3D schematic of the setup and Fig 3.5 (b) shows the photograph of the developed table top setup.

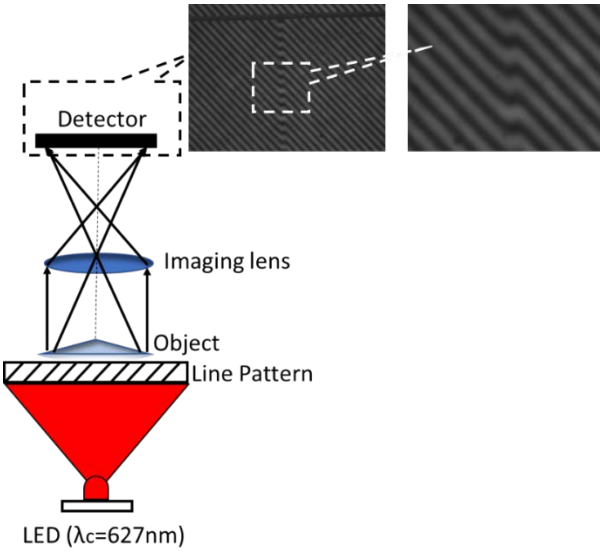


Fig 3.3 Transmission mode FPT for shape measurement of phase objects

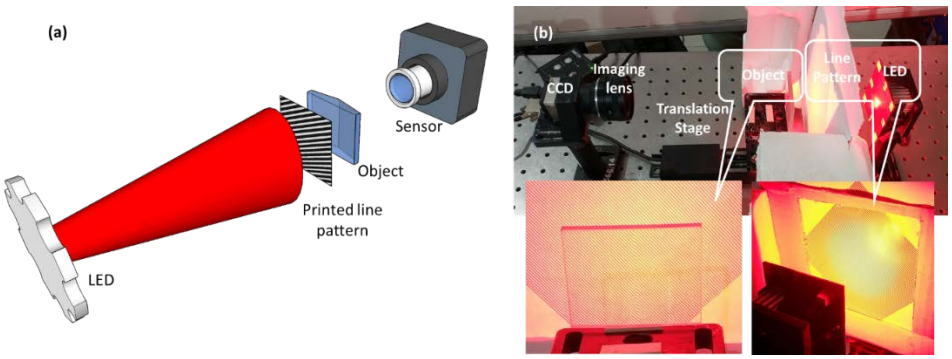


Fig 3.4 (a) 3D schematic of the transmission mode fringe projection device. (b) Photograph of the table-top setup

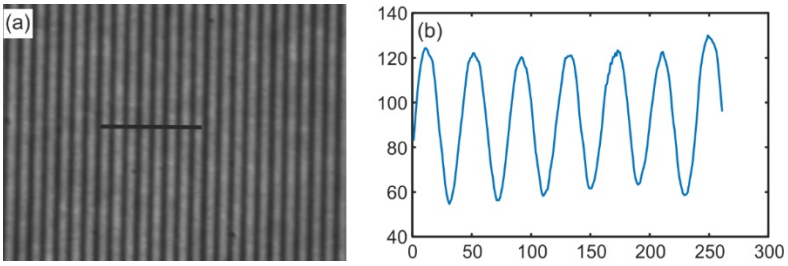


Fig 3.5 (a) Projected line pattern imaged by digital array (b) Variation of intensity pattern along the line shown in fig 3.4 (a)

### 3.4 Simulations

Initially simulations are carried out to ascertain whether the discussed technique is useful in shape measurement of such objects. For the simulations, phase objects of different shapes and thickness were used.

#### 3.4.1 Simulation setup

An optical system with unit magnification of as shown in Fig 3.6 is considered in the simulations. A biprism and a right-angled cone were used as the objects in the simulations.

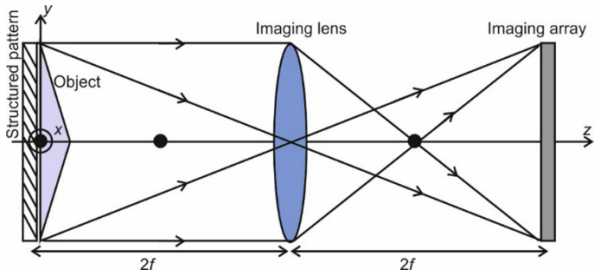


Fig 3.6 Optical system configuration for imaging the structured pattern projected through object under investigation. A magnification of 1 is used in the simulations

The structured pattern was projected through the phase object. The complex amplitude at the object plane ($C_1$) is then given by

$$C_1(x,y,z=0) = A_s \exp\left[i\phi_s(x,y)\right] A_o \exp\left[i\phi_o(x,y)\right] \quad (3.3)$$

Where $A_s$ and $A_o$ are the scalar amplitude distributions and $\phi_s$ and $\phi_o$ are the phases of the structured pattern and object under investigation respectively. This is propagated to the lens plane (situated at a distance of 2f from the object plane) using angular spectrum propagation diffraction integral [21] leading to

$$C_2(x,y,z=2f) = \int_{-\infty}^{\infty}\int \hat{C}_1(x,y,z=0)\, e^{ik\sqrt{1-\lambda^2 f_X^2-\lambda^2 f_Y^2}\,2f}\, e^{i2\pi(f_X x+f_Y y)}\, df_X\, df_Y \quad (3.4)$$

Where, $\hat{C}_1$ is the angular spectrum (frequency spectrum) of the complex amplitude distribution at the object plane obtained by Fourier transforming the complex amplitude distribution $C_1$ at the object plane. Source vacuum wavelength of λ=627nm (which is the peak wavelength of the

LED source used in experiments) with a Δλ=20nm is considered in the simulations. After propagation, just after the lens plane the complex amplitude is presented as

$$C_3(x,y) = C_2(x,y)e^{\left[i\frac{\pi}{\lambda f}\left(x^2+y^2\right)\right]} \tag{3.5}$$

where the exponential function represents a lens of focal length *f*. The angular spectrum integral, whose form is shown in Eq. (3.4), is used to propagate this complex amplitude to the image plane, which is located at a distance of 2*f* from the lens plane. To simulate a quasi-monochromatic source, the above steps are repeated for a band of wavelengths. A total of 100 wavelengths symmetrically distributed about 627nm having a Gaussian spectrum is used to propagate the object complex amplitude distribution to the image plane. To acquire the complex amplitude distribution of the object at the image plane due to the LED source, the complex amplitudes obtained for each wavelength were added (vector addition). The intensity distribution at the image plane is then obtained using

$$I(x,y) = \left|C_I(x,y)\right|^2 + I_{noise} \tag{3.6}$$

Where $I_{\text{noise}}$ represent a 10% Gaussian white noise (10% representing the variance), which is added to the intensity obtained by propagation. This is added to take into consideration noises like non-uniform spatial distribution of the source intensity, non-uniform spatial response of the detector, non-uniform intensity due to printed pattern etc.

### 3.4.2 Simulated objects

Fig 3.7 shows the phase distribution of the bi-prism, which is used as one of the objects in simulations. In the figure, regions with zero grey value represents zero phase and higher grey values represents higher phase and hence higher optical thickness.

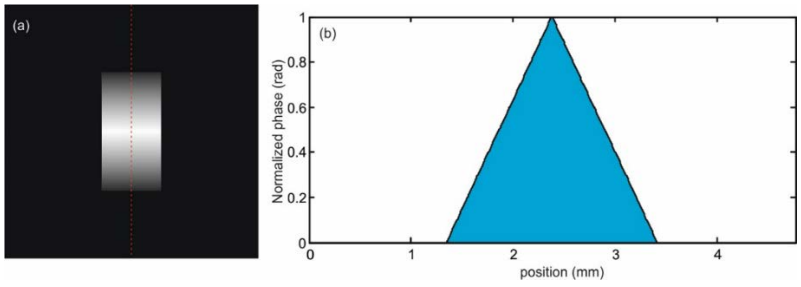


Fig 3.7 Phase of the simulated bi-prism. (a) Phase distribution in false color, where white grey value represents a normalized phase of 1 rad. (b) Normalized phase distribution along the red dotted line in Fig 3.7 (a). This phase is directly proportional to optical path length

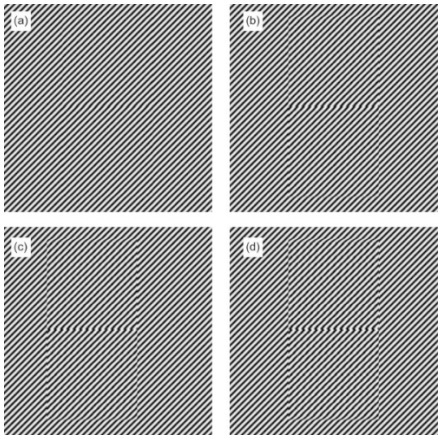


Fig 3.8 Simulated line patterns at the detector array (image plane) for bi-prisms of different optical thicknesses (a) Optical thickness=λ (b) Optical thickness=5λ (c) Optical thickness=7λ and (d) Optical thickness=10 λ ( λ =627nm).

Simulations were carried out for objects with different optical thicknesses (at the highest point). The optical thickness was changed from λ to 10 λ and the corresponding intensity at the image plane were simulated. Fig 3.8 shows the intensity distributions corresponding to four optical height distributions. It can be seen from Fig 3.8 that as the optical thickness increases the deflection of the structured pattern from its original position increases. This deflection can be quantified by analysing the image patterns.

### 3.4.3 Image analysis

Image without the object represents the carrier fringe pattern as it is used to carry data of the object in the form of pattern modulation. The analysis of the fringe pattern can be carried out by a simple Fourier analysis of the recorded structured pattern [71, 72]. The extent of modulation can be quantified by subtracting the phase obtained from the image of the carrier fringe pattern from the image of the modulated interference pattern. The image analysis process is schematically shown in Fig 3.9.

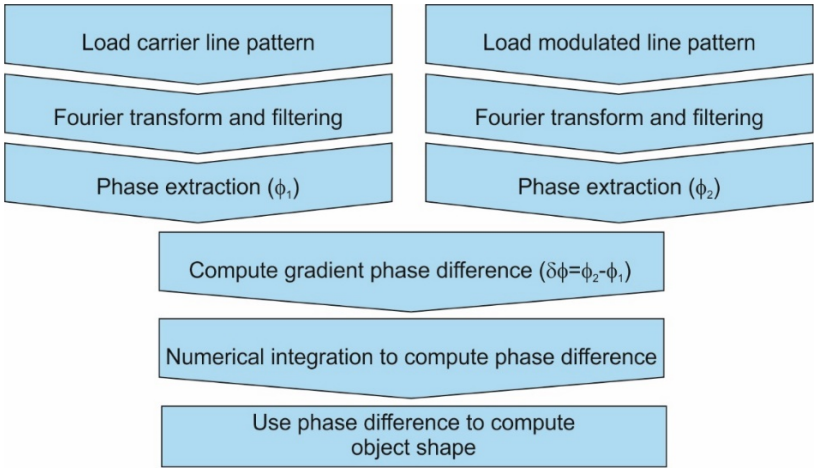


Fig 3.9 Flow chart of the object shape determination process

As written in the previous section, the beam deflection is proportional to the gradient of the optical path length inside the object under investigation. So, the Fourier analysis yields information about the angle of deflection, which in turn needs to be numerically integrated to compute information about optical thickness distribution of the sample. The system should be calibrated first using a sample with known optical thickness distribution and then determining the relationship between the obtained numerically integrated phase and the optical thickness of the sample.

Steps involved in the reconstruction process shown in Fig 3.9 are applied to the line patterns for objects with different optical thickness distributions (Simulated and experimental). Fig 3.10 shows the different steps involved in the determination of the shape (optical thickness distribution) of the object for a bi-prism with maximum optical thickness of 10 λ. Fig 3.10 (a) shows the Fourier spectrum of the recorded modulated line pattern due to the presence of the object. This is then filtered (Fig 3.10 (b)) using a circular mask cantered at one of the side bands. A non-linear filtering using a Gaussian function was adopted to reduce noise in the reconstructed phase distribution. The filtered Fourier spectrum is then inverse Fourier transformed to yield the gradient phase distribution (Fig 3.10 (c)). Profile of the gradient phase along the line in Fig 3.10 (c) is shown in Fig 3.10 (d).

The gradient phase is integrated along the direction of phase variation (in this case y-direction) to convert it into phase. This is shown in Fig 3.10 (e) Phase profiles along different lines (in the y-direction) can be combined to yield the object shape (thickness profile) shown in Fig 3.10 (f). This image reconstruction was carried out on bi-prisms with different optical thicknesses to determine whether the technique maintains a linear relationship between the object thickness

and the reconstructed phase, which is expected. Results of the shape reconstruction for bi-prisms of different optical thickness are shown in Fig 3.11.

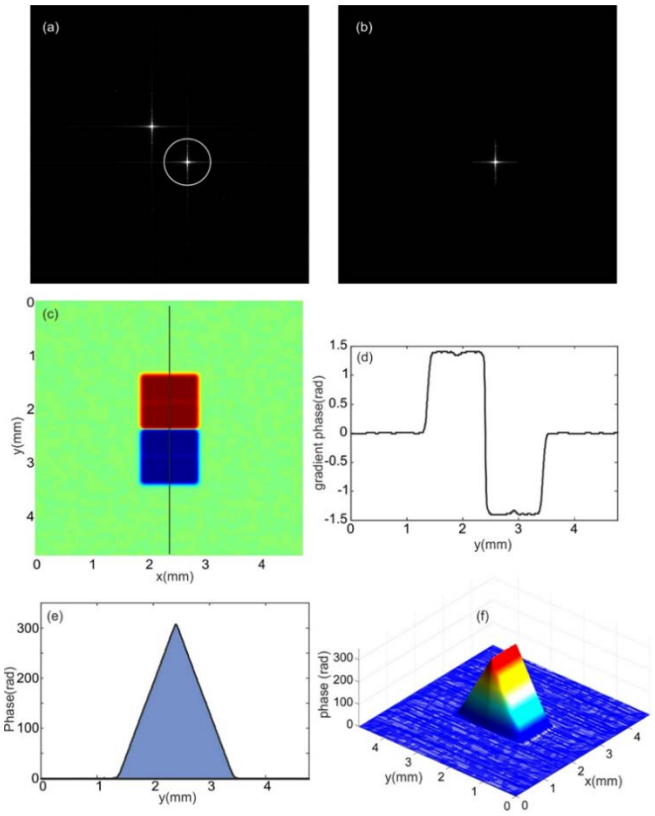


Fig 3.10 simulation results for biprism (a) Fourier spectrum of modulated structured pattern. (b) Filtered Fourier spectrum. (c) Gradient phase difference obtained by subtracting gradient phase due to carrier line pattern from gradient phase due to object line pattern. (d) Gradient phase along the y direction. (e) Phase profile obtained after numerical integration along y-direction. (f) Three- dimensional rendering of object shape profile in terms of obtained phase.

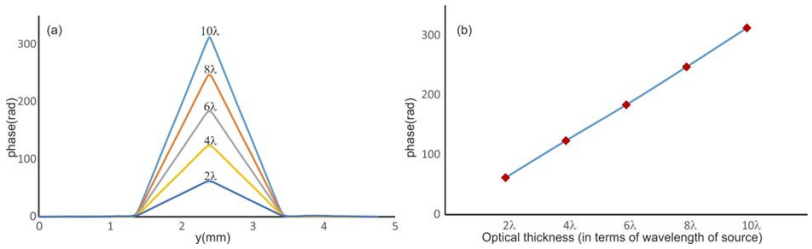


Fig 3.11 (a) Reconstructed phase profile (after numerical integration) for simulated objects as a function of object optical thickness (in terms of wavelength of source). (b) Maximum value of reconstructed phase as a function of object maximum optical thickness.

The change in reconstructed phase has linear dependence upon the optical thickness of the object. So, a calibration plot can be used to convert reconstructed phase to object optical thickness easily. Simulations were then carried out using rectangular cone as the object under investigation. Fig 3.12 shows the simulation results. The maximum phase reconstructed for different optical thickness closely match that obtained for the biprism.

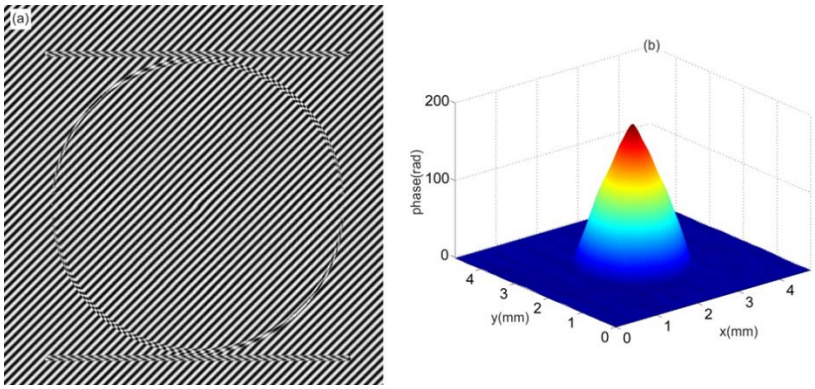


Fig 3. 12 Simulation results with right angular cone as object. (a) Simulated intensity pattern at the detector plane. (b) Reconstructed phase distribution.

From the simulation results it can be seen that the method can be used to reconstruct the shape profiles of transparent phase object. In the case where a calibration object is available, this technique can be used to convert the obtained numerically integrated phase into optical thickness profile of the object also.

### 3.5 Experimental Results of Shape reconstruction of Phase Objects

The experiments were performed in two sets. The first set was performed with CCD camera as sensor and the second set with smartphone camera. Smartphone camera is used as recording device to demonstrate the potential of this technique to be developed into portable instrument. The phase objects used for observation are bi-prism, cylindrical rod and cylindrical lens. Fig 3.13(a) and 13(b) show the line pattern recorded by a CCD camera (Thorlabs, 4.65μm pixel pitch, 8-bit dynamic range) projected through a biprism (179° angle, 4cm x 5cm), with and without bi-prism in FOV, respectively. Fourier analysis of the distorted and undistorted patterns. After numerical phase subtraction, we get the gradient phase profile, as shown in Fig 3.13(c). This is numerically integrated along the direction of variation to recover the 3D rendering of shape of the bi-prism shown in Fig 3.13(f). Fig 3.13(e) shows the cross-sectional view of the object after numerical integration of gradient phase.

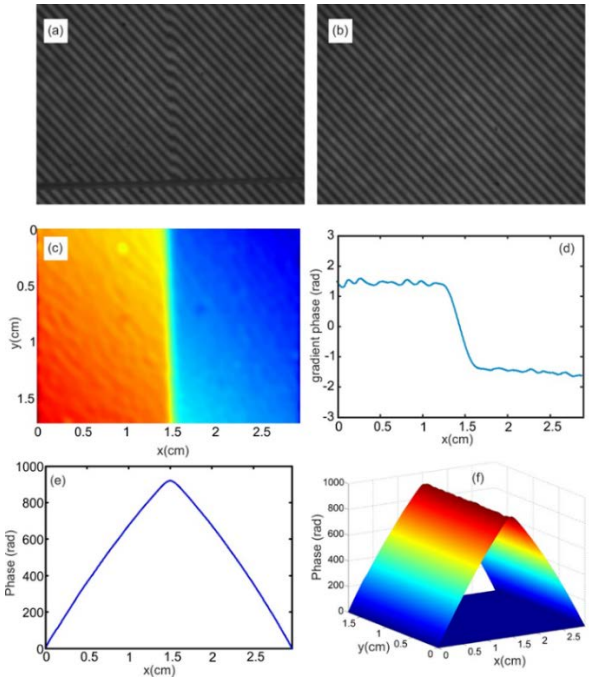


Fig 3.13 Results of shape reconstruction with biprism as the object using a 4.65μm pixel pitch CCD array as the recording device (a) Image of the line pattern recorded with the biprism placed in the field of view. (b) Image of the same line pattern recorded after removing the biprism (reference pattern). (c) Obtained gradient phase profile of the object after phase subtraction. (d) Line profile of the gradient phase. (e) Cross-sectional shape profile of the object after numerical integration of gradient phase. (f) Three-dimensional rendering of the shape of the bi-prism in terms of the recovered phase (obtained after numerical integration along each line along which there is variation in gradient phase).

The experiment is also carried out for a glass cylindrical rod. Experimental procedure is the same as in the case of biprism and results obtained are shown in Fig 3.14. The image recorded with and without object in FOV are shown in Fig 3.14(a) and fig 3.14(b). The phase gradient profile of object can be seen in Fig 3.14(c). The cross-sectional shape of object after numerical integration and the 3D shape rendering with respect to recovered phase is shown in Fig 3.14(e) and 3.14(f) respectively. Similar experiment was carried out for cylindrical lens with CCD camera as recording device. Only a half the FOV is covered by lens. The results are shown in Fig 3.15.

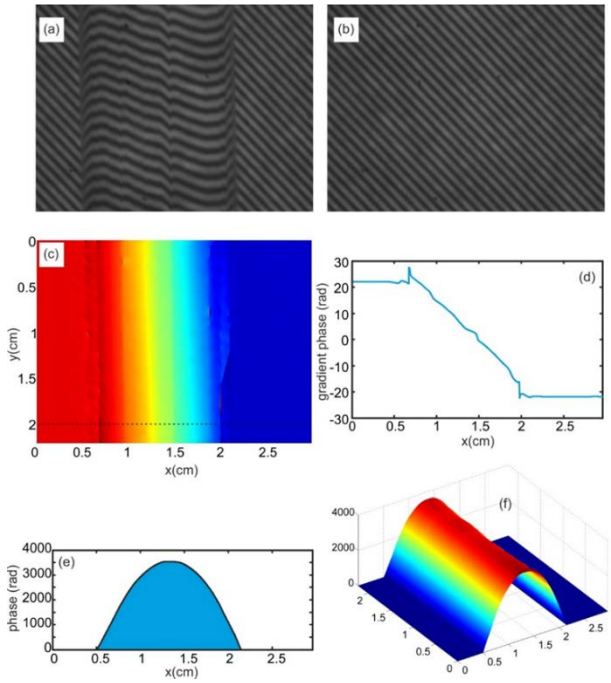


Fig 3.14 Results of shape reconstruction for a cylindrical rod. Recording device was CCD camera (a) Image of the line pattern recorded with the rod placed in the field of view. (b) Image of the same line pattern recorded after removing the rod (reference pattern). (c) Obtained gradient phase profile of the object after phase subtraction. (d) Line profile of the gradient phase. (e) Cross-sectional shape profile of the object after numerical integration of gradient phase. (f) 3D rendering of the shape of the cylinder in terms of the recovered phase.

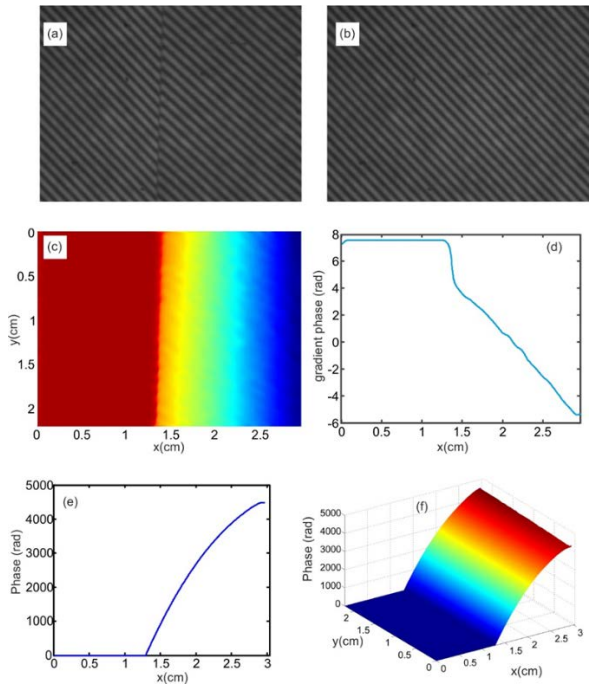


Fig 3.15 Results of shape reconstruction for a cylindrical lens as the object. Recording device was CCD camera. Only half the field of view is covered by the lens. (a) Image of the line pattern recorded with the lens placed in the field of view. (b) Image of the same line pattern recorded after removing the lens (reference pattern). (c) Obtained gradient phase profile of the object after phase subtraction. (d) Line profile of the gradient phase. (e) Cross-sectional shape profile of the object after numerical integration of gradient phase. (f) Three-dimensional rendering of the shape of the cylindrical lens in terms of the recovered phase.

The same set of experiments explained above are also performed using smartphone camera as sensor. The experiment is conducted on bi-prism and cylindrical rod used for experiment above. The results for bi-prism, cylindrical rod and cylindrical lens are shown in Fig 3.16, Fig 3.17 and Fig 3.18 respectively. As we can see, the shape rendered in case of CCD camera and smartphone camera are comparable.

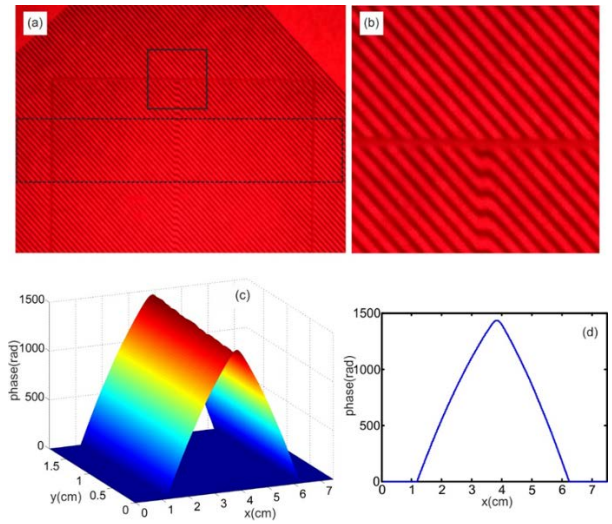


Fig 3.16 Results of shape reconstruction for a bi-prism. Recording device was a smart-phone camera. (a) Image of the line pattern recorded with the bi-prism placed in the field of view. (b) Image of the same line pattern recorded after removing the bi-prism (reference pattern). (c) Three-dimensional rendering of the shape of the bi-prism lens in terms of the recovered phase. (d) Cross-sectional shape profile of the object

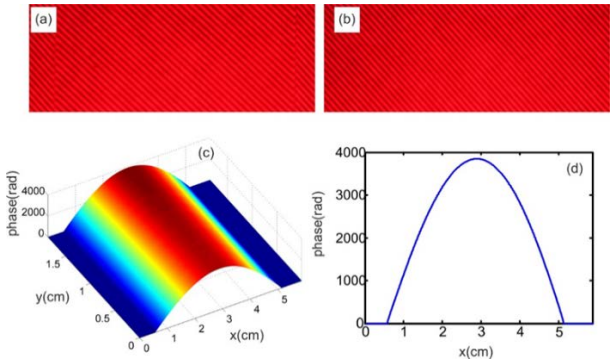


Fig 3.17 Results of shape reconstruction for a cylindrical rod. Recording device was a smart-phone camera. (a) Image of the line pattern recorded with the cylindrical lens placed in the field of view. (b) Image of the same line pattern recorded after removing the lens (reference pattern). (c) Three-dimensional rendering of the shape of the cylindrical lens in terms of the recovered phase. (d) Cross-sectional shape profile of the object.

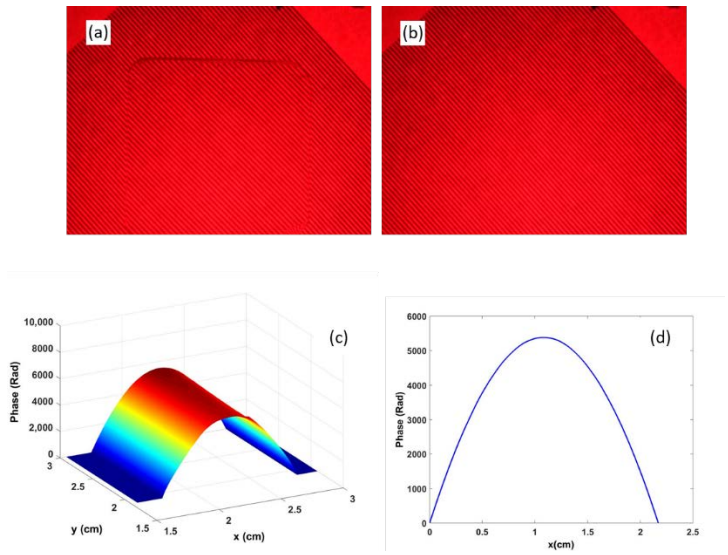


Fig 3.18 Results of shape reconstruction for a cylindrical lens. Recording device was a smart-phone camera. (a) Image of the line pattern recorded with the cylindrical lens placed in the field of view. (b) Image of the same line pattern recorded after removing the lens (reference pattern). (c) Three-dimensional rendering of the shape of the cylindrical lens in terms of the recovered phase. (d) Cross-sectional shape profile of the object.

The experiments described shows that the projection of structured patterns through phase objects could be used for the extraction of the shape of the objects. It is definitely possible to use such a technique in shape measurement and dynamic studies of phase micro-objects including living cells.

### 3.6 Fringe projection microscope in transmission mode

Transmission mode fringe projection technique is then used in microscopy for three-dimensional shape measurement and dynamic studies of micro-objects including human Red Blood Cells (RBC). Fig 3.19 shows the schematic of the developed microscope. Light from an LED with central wavelength λ of 627nm and output power of 2W was utilized as the light source. This light travels through a ground glass diffuser to get spatially uniform illumination. This is then reflected by a set of parallel lines of pitch 250 µm printed on photo paper. The lines were printed using an inkjet printer providing 2880dpi resolution. Intensity variation across the pattern was sinusoidal in nature. A condenser lens (MO with 45x magnification and NA=0.65) is used to project the image of the line pattern through the object. The condenser lens increases the spatial density of the printed pattern by reducing the pitch of the fringe to around 5 µm. The fringe pattern projected through the object is then imaged onto a webcam sensor (VGA, 3.2 µm pixel pitch) using a MO (40x, NA=0.65). The object distorts the fringe pattern due to spatially varying optical thickness, so that the projected straight-line pattern is modulated wherever object is present and there is a spatially varying optical thickness. The line pattern deformation is quantified using Fourier fringe analysis method discussed in the

previous sections [258,259]. Fringe patterns are recorded with and without the object present in the FOV. To get the phase due to object alone, subtract the phase information obtained from the numerical processing of the patterns without the object present in the FOV from the phase information obtained from the pattern recorded with the object present in the FOV. This procedure also reduces unwanted phase caused by optical system aberrations.

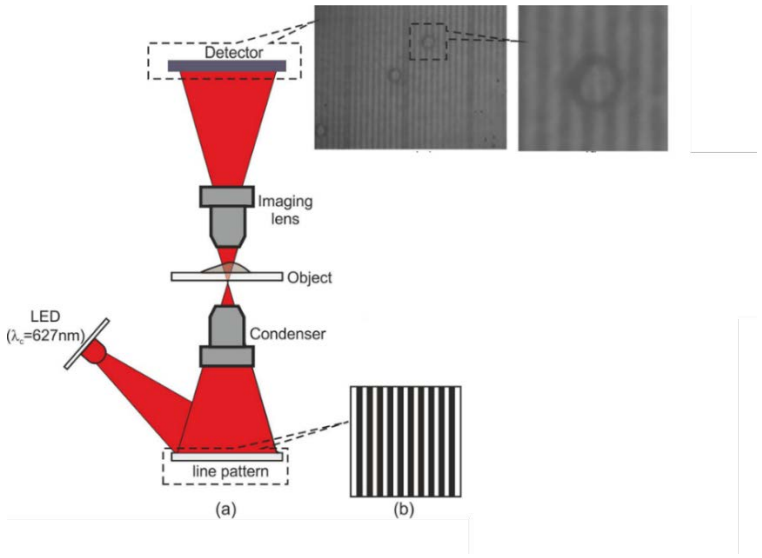


Fig 3.19 (a) Transmission mode quantitative 3D fringe projection microscope. (b) schematic representation of the line pattern.

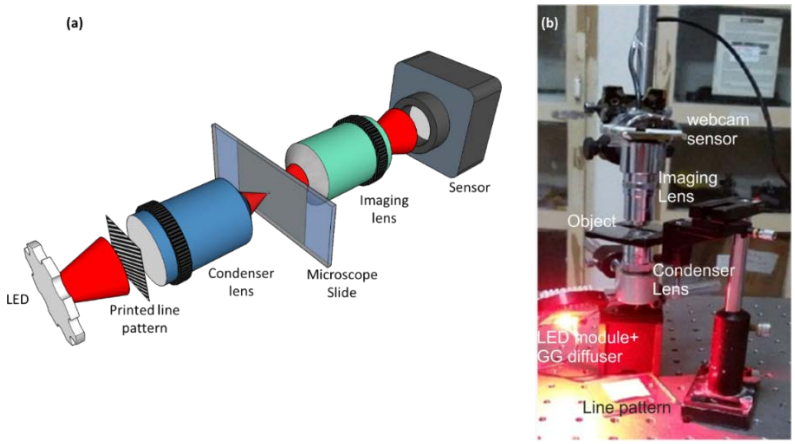


Fig 3.20 (a) shows the 3D schematic of the developed system (b) shows the photograph of the developed system with different parts marked. The web cam was mounted near to the objective lens and so the magnification is around 15x. This was measured using microspheres of known size.

### 3.7 Experimental results of shape measurement of micro-objects

First set of experiments were performed on a dispersion of 10 µm diameter (RI of 1.58 at 586 nm) polystyrene micro-spheres in distilled water. Fig 3.21 (a) and 3.21 (b) shows the projected

line patterns recorded by the sensor, with and without the object present in the FOV respectively. The recorded line patterns are Fourier transformed to yield the spatial frequency spectrum which is shown in Fig 3.21 (c) and 3.21 (d). The filtering is applied using the circular window shown in Fig 3.22 (c) and 3.22 (d). These are then inverse Fourier transformed and the phase difference is computed which is shown in Fig 3.21 (e). Fig 3.21 (f) shows the gradient phase along the direction of variation (horizontal) of the projected line pattern after unwrapping the phase distribution inside the window shown in Fig 3.21 (e) using Goldstein branch cut method. It can be seen that gradient phase along the direction (horizontal) of the projected line pattern is obtained (Fig 3.21(f)). This is numerically integrated along the horizontal direction to yield the phase information. The three-dimensional rendering of the spatially varying phase provides the thickness distribution of the object as shown in Fig 3.21 (h). It can be seen that the shape resembles that of a sphere.

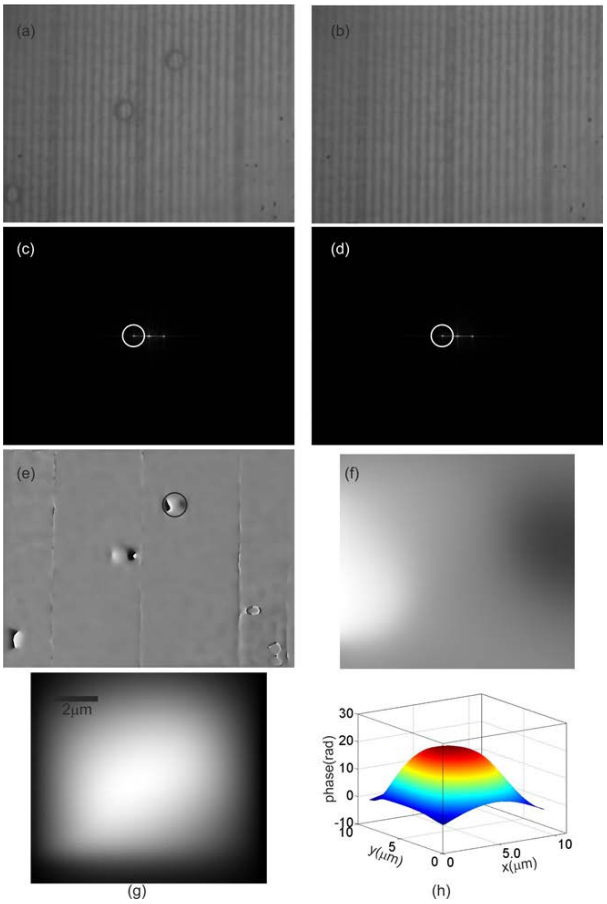


Fig 3. 21 Recorded line patterns (a) with and (b) without the object in the field of view. Spatial frequency spectrum (c) with object and (d) without object in the field of view. (e) Wrapped gradient phase obtained after phase subtraction. (f) Obtained gradient phase after phase unwrapping. (g) Phase obtained after numerical integration along horizontal direction. (h) Three-dimensional thickness distribution as a function of phase.

The next set of experiments were carried out to examine the dynamic behaviour of human erythrocytes. Thin blood smears were made on a microscope slide and covered with a cover

slip for this experiment. This is placed in the microscope and adjusted to get the image of the cells together with the projected line pattern at the detector plane. Fig 3.22 shows the recorded images for red blood cells. For phase comparisons, the pattern was also recorded without the object in the FOV. Fig. 23 (a) shows the obtained gradient phase and Fig 3.23 (b) shows the computed shape of the cell after numerical integration of the gradient phase along the vertical direction.

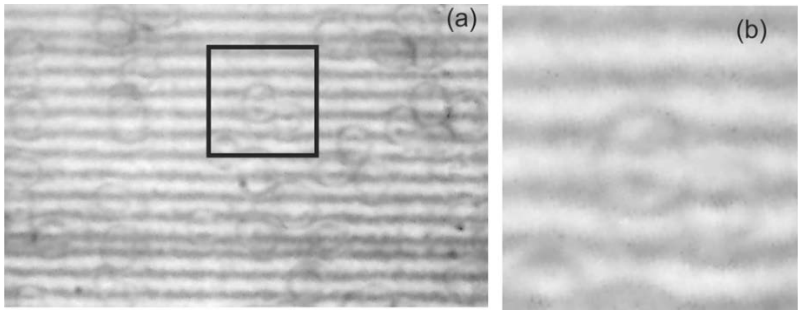


Fig 3. 22 (a) Recorded image for red blood cells. (b) Portion inside the rectangular box showing the modulation of the line pattern

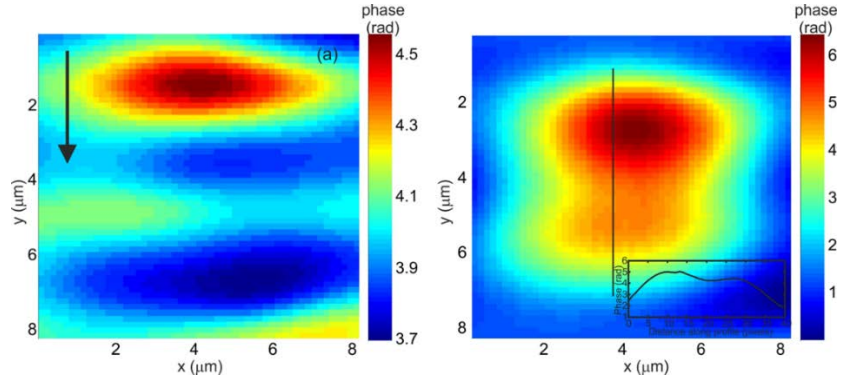


Fig 3. 23 Quantitative imaging of human red blood cells. (a) unwrapped gradient phase profile. (b) Computed cell shape after numerical integration. Arrow in Fig 3.23 (a) shows direction of integration. The inset in Fig 3.23 (b) shows the cross-sectional profile of phase variation along the vertical line which indicated the donut profile of the cell.

For imaging of cell dynamics, a time series of line patterns projected through the cells is recorded. Before studying the dynamics of cells, the temporal stability of the system, which will define the minimum temporal variation in phase that can be resolved is measured. Since cells like red blood cells fluctuate with amplitudes of few tens of nano-meters, temporal stability of the order of a nano-meter is required to image their dynamics. For measuring the temporal stability, a blank slide was placed in the microscope. Image of the line pattern was recorded at the rate of 2 Hz for 60 seconds (total of 120 frames). The gradient phase from the

line pattern at each time instant is subtracted from the gradient phase reconstructed from the line pattern at time t=0s. These gradient phase maps were then unwrapped and integrated along the direction of variation of the line pattern to get the phase profile. The temporal ability of the setup was computed form the mean of the temporal standard deviation of 2500 random spatial points in the phase map. The stability was found to be 0.0194 radians over a period of 60s. Fig 3.24 shows the histogram of the standard deviation of the phases obtained from 2500 random points.

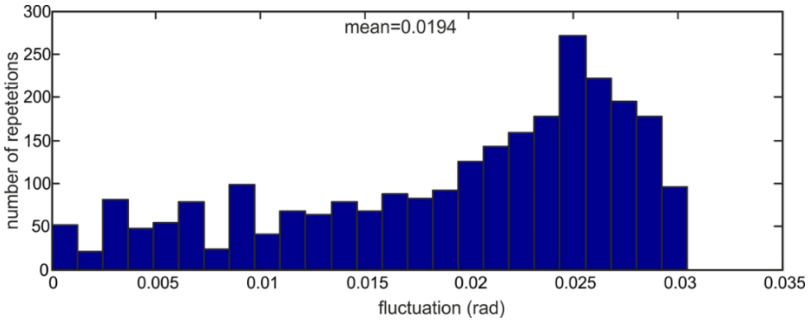


Fig 3. 24 Temporal stability of the setup

This value of phase for the temporal stability is equal to around 2.1nm in terms of path length variation. This is slightly on the higher side compared to some of the self-referencing and common path interference techniques [61,64,65,79,80,260]. But it should be noted here that the developed technique is non-interferometric in nature, without the need for interference or spatial filtering of the source. This stability might be enough to measure the membrane fluctuations of red blood cells. For fluctuation measurement of red blood cells, 120 frames at 2 Hz were recorded for each sample. They were numerically processed to yield the gradient spatial phase distribution at each instant of time. Reference gradient phase was subtracted from object phase at each instant of time and numerical integration was done to obtain the time varying phase profiles. The fluctuation profile of the cell under investigation is determined by the temporal standard deviation of the profile. Fig. 3.26 shows the phase profile of the cell at four- time instances.

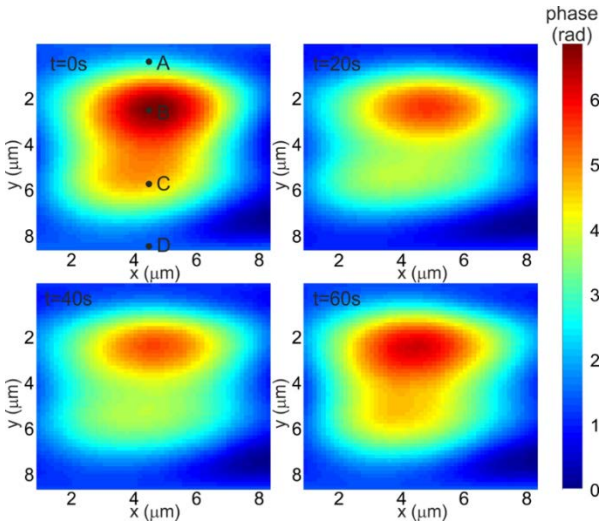


Fig 3. 25 Phase profile of a healthy human red blood cell at different time instances. Time variation of the phase profiles at the points on the phase map at t=0s are computed and is shown in Fig 3.26

The measured fluctuations fall within the temporal phase resolution of the system, which makes the present technique useful for the imaging of cell thickness fluctuations. This can be seen from Fig 3.35 and Fig 3.26, which shows that the technique provides accurate enough measurement of the thickness variations. Also, Fig 3.26 shows the standard deviation (nm) and also indicates that the fluctuations is spatially varying, which has been reported earlier in the literature. This figure also shows that the fluctuations of the background (point D, which was outside the cell) are negligible in comparison to the points inside the cell (A to C), which is as anticipated [27].

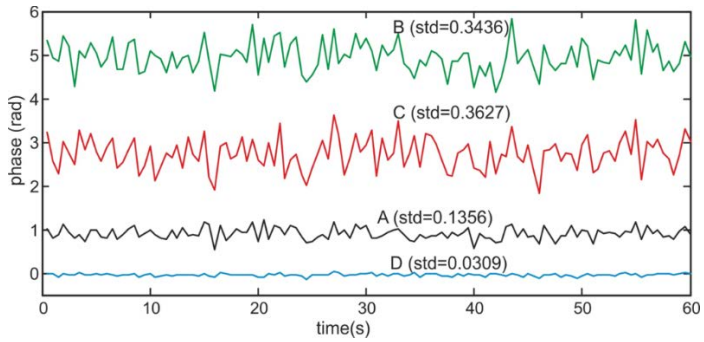


Fig 3. 26 time evolution of the phase profile at different spatial points along with their standard deviation (fluctuation).

## 3.8 Conclusion

An effective and easy to implement technique for 3-dimensional shape measurement of phase objects (macro and micro) has been demonstrated. A set of parallel lines printed on a paper is projected through the object under investigation. The line pattern is modulated due to the spatially varying optical thickness distribution of the object. This modulation is proportional to

the gradient of optical thickness at each point. The modulation is quantified by Fourier fringe analysis and the phase profile is obtained after numerical integration, yielding the thickness profile of the object under investigation. Since the fringe projection technique does not rely on the generation of interference fringes, it requires only few optical components compared to interferometric techniques making the system easy to implement and immune to mechanical vibrations. The experiments performed in the first part of the work are in agreement with the simulations. The set of experiments have been performed with both CCD and a smart phone camera sensor which depicts that a portable handheld and a user-friendly device can be made out of the table top setup. We can infer from the results that fringe projection technique can be used for surface mapping of optical components and can be implemented in industries dealing with optical testing.

Fringe projection technique has also been employed in transmission mode for retrieving the 3-dimensional information of polystyrene beads and human erythrocytes (RBCs). The temporal stability of the system is found to be 2.1nm which is of the same range as that of interferometric techniques. The technique yields the bio-physical and bio-mechanical parameters of the RBCs which were found consistent with the values reported in literature. The future scope of this work is to use a grid structured pattern to be projected to obtain simultaneous horizontal and vertical shape measurement. Moreover, the technique can be implemented in studying the dynamic properties of the cells for characterization of cells.

Fringe projection technique offers certain advantage over interferometry techniques such as its ease of implementation, its simple, compact and inexpensive configuration, and no need of stringent beam alignment, it still has some drawbacks. It gives gradient phase of the objects. Moreover, the phase sensitivity of the fringe projection technique is less than interferometric techniques. Therefore, in the upcoming chapters, we have explored interferometric techniques for the quantitative phase contrast imaging of human erythrocytes.